

Molecular Clouds Toward the Super Star Cluster NGC3603; Possible Evidence for a Cloud-Cloud Collision in Triggering the Cluster Formation

Y. Fukui¹, A. Ohama¹, N. Hanaoka¹, N. Furukawa^{1,2}, K. Torii¹, J. R. Dawson³, N.
Mizuno⁴, K. Hasegawa¹, T. Fukuda¹, S. Soga¹, N. Moribe¹, Y. Kuroda¹, T. Hayakawa¹, A.
Kawamura⁴, T. Kuwahara¹, H. Yamamoto¹, T. Okuda^{1,4}, T. Onishi,⁵ H. Maezawa⁵, and
A. Mizuno⁶

fukui@a.phys.nagoya-u.ac.jp

Received _____; accepted _____

Version 2013-05-16

¹Department of Astrophysics, Nagoya University, Chikusa-ku, Nagoya, 464-8602, Japan

²present address: Center for Astronomy, Ibaraki University, 2-1-1 Bunkyo, Mito, Ibaraki
310-8512, Japan

³School of Mathematics and Physics, University of Tasmania, Sandy Bay Campus,
Churchill Avenue, Sandy Bay, TAS 7005

⁴National Astronomical Observatory of Japan, Mitaka, Tokyo, 181-8588, Japan

⁵Department of Astrophysics, Graduate School of Science, Osaka Prefecture University,
1-1 Gakuen-cho, Sakai, Osaka 599-8531, Japan

⁶Solar-terrestrial Environment Laboratory, Nagoya University, Chikusa-ku, Nagoya, 464-
8601, Japan

ABSTRACT

We present new large field observations of molecular clouds with NANTEN2 toward the super star cluster NGC3603 in the transitions $^{12}\text{CO}(J=2-1, J=1-0)$ and $^{13}\text{CO}(J=2-1, J=1-0)$. We suggest that two molecular clouds at 13 km s^{-1} and 28 km s^{-1} are associated with NGC3603 as evidenced by higher temperatures toward the H II region as well as morphological correspondence. The mass of the clouds is too small to gravitationally bind them, given their relative motion of $\sim 20\text{ km s}^{-1}$. We suggest that the two clouds collided with each other a Myr ago to trigger the formation of the super star cluster. This scenario is able to explain the origin of the highest mass stellar population in the cluster which is as young as a Myr and is segregated within the central sub-pc of the cluster. This is the second super star cluster along side Westerlund2 where formation may have been triggered by a cloud-cloud collision.

Subject headings: ISM: clouds — open clusters and associations — individual:
(NGC3603)

1. INTRODUCTION

High-mass stars dynamically agitate and ionize the interstellar medium in galaxies through strong radiation, stellar winds and, eventually, supernova explosions. For example, the ultraviolet photons emitted from high-mass stars heat up cold molecular clouds and may inhibit star formation (e.g., Whitworth 1979; Franco et al. 1994). On the other hand, compressive effects such as the expansion of H II regions and supernova explosions can collect diffuse gas to enhance star formation (e.g., Elmegreen & Lada 1977; Hosokawa & Inutsuka 2006). These feedback effects play an important role in regulating star formation in galaxies.

High-mass stars must be formed rapidly in dense molecular clumps in order to overcome the feedback effects from forming stars such as radiation pressure which inhibits mass accretion (Tan & McKee 2004). The alternative scenario of stellar merging requires unreasonably large stellar densities of $\sim 10^8 \text{ Mpc}^{-3}$ (Bonnell et al. 1998) and is not feasible in high-mass star formation in most galaxies. Elmegreen (1998) outline three mechanisms by which the formation and collapse of dense clumps in giant molecular clouds (GMCs) may be dynamically triggered by external events. The first is globule squeezing, in which pre-existing dense clumps are compressed, either by high ambient pressures in H II regions, or by shock-waves propagating from supernovae or other disturbances. The second is “collect and collapse”, in which gas accumulated into a shell or ridge by expanding H II regions, stellar winds or supernovae collapses to form new dense clumps and stars. The third is cloud-cloud collisions, where two molecular clouds collide leading to star formation via gravitational instabilities.

Most high-mass stars are formed in stellar clusters. Super star clusters (SSCs) are the most massive clusters in the Galaxy, with stellar densities exceeding $10^4 \text{ stars pc}^{-3}$ in their cores (Johnson 2005). There are several known SSCs in external galaxies. For example,

R136 in the Large Magellanic Cloud (Hunter et al. 1995b; Massey & Hunter 1998) and NGC 604 in M33 (Hunter et al. 1995a; Maíz-Apellániz et al. 2004).

In addition, the two colliding Antennae galaxies NGC4038 and NGC4039 have young massive star clusters of 10^5 – $10^6 M_{\odot}$, distributed across several kpc (Wilson et al. 2000). Collisions between galaxies will accumulate the ISM in a compact region leading to the formation of gravitationally unstable dense clumps, and it is likely that such a collision can trigger massive cluster formation. It is however difficult to resolve the distribution of the parent molecular clouds in the Antennae galaxies because of their large distance, 20 Mpc. The detailed mechanism of SSC formation is therefore still a mystery because detailed observations of the parent clouds are not available at a sufficiently high spatial resolution. Within the Milky Way there are 8 known young SSCs with an age of a few Myrs (Portegies Zwart et al. 2010). They are the Arches, Quintuplet, RCW38, Westerlund 2, Tr14, NGC3603, Westerlund 1 and [DBS2003]179; in four of them (the Arches, Quintuplet, Tr14 and Westerlund 1) their parent molecular clouds appear to have been dissipated already due to stellar winds and/or ultraviolet photons (UV) (see Table 1). In the remaining four SSCs (RCW38, Westerlund 2, NGC3603 and [DBS2003]179) we see signs of associated nebulosity at infrared wavelengths, and they are good candidates for identifying parent clouds.

Furukawa et al. (2009a) and Ohama et al. (2010) presented observational evidence that a cloud-cloud collision may have triggered the formation of the SSC Westerlund 2. These authors report two GMCs centered at 4 km s^{-1} and 16 km s^{-1} . They argue that acceleration by stellar winds from Westerlund 2 is insufficient to explain the entire observed velocity dispersion of the molecular gas, and suggest a scenario in which a collision between the two clouds may have triggered the formation of the SSC. Theoretical studies have modelled the triggering of star formation via cloud-cloud collisions (Habe & Ohta 1992; Anathpindika

2010), and such collisions are believed to be frequent in gas-rich galaxies (Tasker & Tan 2009).

Following the molecular line studies on Westerlund 2, this paper focuses on NGC 3603 which is similar in stellar age and mass. NGC 3603 is located at $(l, b)=(291^\circ 6, -0^\circ 5)$, close to the tangent of the Carina spiral arm. Discovered by Sir John Herschel in 1834, it is known at present as one of the most massive clusters in the Milky Way (Goss & Radhakrishnan 1969; Walborn 1973; Moffat 1983). The estimated age of the cluster is 1 – 2 Myr (e.g., Sung & Bessell 2004; Harayama et al. 2008) and the total stellar mass has been estimated to be $1.0 - 1.6 \times 10^4 M_\odot$ (Harayama et al. 2008) and $1.76 \pm 0.38 \times 10^4 M_\odot$ (Rochau et al. 2010). This rich stellar population includes more than 30 O type stars (Moffat et al. 2004) and several Wolf-Rayet (WR) stars (Schmutz & Drissen 1999) producing a Lyman continuum flux of $1.5 \times 10^{39} \text{ erg s}^{-1}$ (Kennicutt 1984; Drissen et al. 1995), corresponding to about 100 times the ionizing power of the Orion Trapezium cluster. NGC 3603 is therefore an ideal experimental laboratory in which to study a galactic prototype of the starburst clusters that are observed in the other galaxies. The distance of NGC 3603 has been estimated to be 6.1 – 6.3 kpc (Goss & Radhakrishnan 1969; de Pree et al. 1999; Pandey et al. 2000; Stolte et al. 2004), 7.0 – 7.3 kpc (Moffat 1983; van den Bergh 1978; Caswell & Haynes 1987; Melnick et al. 1989) and as high as 8 or even 10 kpc (Goss & Radhakrishnan 1969; Moffat 1974; Crowther & Dessart 1998). In the present work we shall adopt a distance of 7 kpc, the mean of the published values.

Only a few molecular line observations of the NGC 3603 region have been reported to date. Grabelsky et al. (1988) carried out a large-scale $^{12}\text{CO}(J=1-0)$ observations of the Carina region at a $8''.8$ resolution and identify a molecular cloud at 15 km s^{-1} toward NGC3603 listed as cloud No. 17. The total molecular mass of the cloud is $4 \times 10^5 M_\odot$. These authors also identified another cloud near NGC3603 at 29 km s^{-1} (No. 18), with an estimated

molecular mass of $1 \times 10^5 M_{\odot}$. CS observations by Nürnberger et al. (2002) showed that there are 13 massive molecular clumps around 15 km s^{-1} in the NGC3603 region. Most recently, Röllig et al. (2011) used NANTEN2 to make $\text{CO}(J=4-3)$ observations of NGC3603 for an area of $2' \times 2'$ in l and b and revealed that two molecular clumps at 13 km s^{-1} , MM1 and MM2, are associated with two pillars with photo dissociation region (PDRs) observed by the HST (Brandner et al. 2000). NGC 3603 ionizes an extensive and luminous H II region, RCW57B, with the Wolf-Rayet star WR HD97950 at its center (Hofmann et al. 1995). The intensive radiation and stellar winds from the cluster shape large gaseous pillars (Brandl et al. 1999) at the edge of the cloud (Brandner et al. 2000). There is also another H II region, NGC3576, located 0.4 degrees to the southwest of NGC3603, and its associated molecular cloud is listed as No. 20 in Grabelsky et al. (1988). However, NGC3576 is on the near side of the Carina arm at a distance of 3.0 kpc and is not related to NGC3603 (de Pree et al. 1999).

In this paper, we present new $\text{CO}(J=2-1)$ and $(J=1-0)$ observations of NGC3603 with NANTEN2, and an analysis of this molecular data set. Section 2 describes the observations. Section 3 presents the molecular data and in Section 4 we discuss the formation of the super star cluster. Conclusions are summarized in Section 5.

2. OBSERVATIONS

Observations of the $J=2-1$ transition of CO were made with the NANTEN2 4 m sub-millimeter telescope of Nagoya University at Atacama (4865 m above sea level) in October-November 2008 for $^{12}\text{CO}(J=2-1)$ and in October 2009 for $^{13}\text{CO}(J=2-1)$. The half-power beam width (HPBW) of the telescope was $90''$ at 230 GHz. The 4 K cooled superconductor-insulator-superconductor (SIS) mixer receiver provided a typical system temperature of $\sim 200 \text{ K}$ in a single-side band at 220 – 230 GHz, including the atmosphere

toward the zenith. The spectrometer was an acousto-optical spectrometer (AOS) with 2048 channels, providing velocity coverage of 392 km s^{-1} at 230 GHz. The pointing was checked regularly by observing the radio continuum emission from Jupiter, and was accurate to within $10''$. The target region was observed between elevation angles of 30° and 60° . We observed a large area surrounding NGC 3603 in $^{12}\text{CO}(J=2-1)$, while $^{13}\text{CO}(J=2-1)$ observations are limited to a smaller region (see Figure 1). The OTF (on-the-fly) mapping mode was used in the observations, and the output grid of the region is $30''$. We smoothed the velocity and spatial resolutions to 0.19 km s^{-1} and $100''$, respectively, to achieve a better noise level. Finally, we obtained rms noise fluctuations of $\sim 0.2 \text{ K}$ and $\sim 0.1 \text{ K}$ per channel in $^{12}\text{CO}(J=2-1)$ and $^{13}\text{CO}(J=2-1)$, respectively. The standard sources Ori KL (α, δ)_{J2000}=($5^{\text{h}} 32^{\text{m}} 14^{\text{s}}.5, -5^\circ 22' 27''.6$) for $^{12}\text{CO}(J=2-1)$ and ρ Oph East (α, δ)_{J2000}=($16^{\text{h}} 32^{\text{m}} 22^{\text{s}}.56, -24^\circ 28' 31''.8$) were observed for intensity calibration for $^{13}\text{CO}(J=2-1)$ every 2 hours. We assumed true main beam temperatures, T_{MB} , of $75 - 83 \text{ K}$ in $^{12}\text{CO}(J=2-1)$ as observed by the KOSMA telescope (Schneider et al. 1998) and 17 K in $^{13}\text{CO}(J=2-1)$ as observed by the 60 cm Survey telescope (Nakajima et al. 2007).

Observations of the $^{12}\text{CO}(J=1-0)$ and $^{13}\text{CO}(J=1-0)$ transitions were made with NANTEN2 telescope during September to November 2011. The observations were carried out with a 4 K cryogenically cooled Nb SIS mixer receiver. The typical system temperature was $\sim 270 \text{ K}$ in the double-side band. Two digital spectrometers provided a bandwidth and resolution of 1 GHz and 61 kHz , which corresponds to 2600 km s^{-1} with velocity resolution of 0.17 km s^{-1} , respectively, at 110 GHz . The pointing was checked regularly on the Sun by radio continuum emission. The HPBW of the telescope was $2'.6$. Observations of $^{12}\text{CO}(J=1-0)$ and $^{13}\text{CO}(J=1-0)$ were simultaneously made in the OTF mode with a $1'$ grid spacing. We smoothed the velocity and spatial resolutions to 0.66 km s^{-1} and $163''$, respectively. Finally, we obtained rms noise fluctuations of $\sim 0.3 \text{ K}$ and $\sim 0.2 \text{ K}$ per channel in $^{12}\text{CO}(J=1-0)$ and $^{13}\text{CO}(J=1-0)$, respectively. We used the standard sources Ori KL ($\alpha,$

$\delta)_{J2000}=(5^{\text{h}} 32^{\text{m}} 14^{\text{s}}.5, -5^{\circ} 22' 27''.6)$ for $^{12}\text{CO}(J=1-0)$ and $^{13}\text{CO}(J=1-0)$.

3. RESULTS

3.1. Morphological and Kinematic Analysis

Figure 1 shows the large scale $^{12}\text{CO}(J=1-0)$ distribution toward NGC3603, including only the positive velocity clouds on the far side of the Carina arm (Mizuno & Fukui 2004). NGC3603 is located between the two brightest peaks of $^{12}\text{CO}(J=1-0)$ in the center of Figure 1. Figures 2 – 5 show the velocity channel distributions of the $^{12}\text{CO}(J=2-1)$, $^{13}\text{CO}(J=2-1)$, $^{12}\text{CO}(J=1-0)$ and $^{13}\text{CO}(J=1-0)$ emission, respectively. The velocity range of these figures (from 3.2 km s^{-1} to 34.7 km s^{-1}) was chosen to include all features in the vicinity of NGC3603. The bright CO cloud peaked at around 13 km s^{-1} (cloud No. 17, Grabelsky et al. 1988) has two peaks on the north and south of NGC3603, and is obviously associated with NGC3603 and the other weak CO features at around 28 km s^{-1} are additional candidates for associated clouds (cloud No. 18, Grabelsky et al. 1988). We name the former the blue-shifted cloud and the latter the red-shifted cloud. The blue-shifted cloud is compact and intense, while the red-shifted cloud is extended and weak. We give the parameters toward the two peaks of the two clouds in Table 2. The molecular column density is generally ten-times higher in the blue-shifted cloud than in the red-shifted cloud.

Figures 6 a and b show $^{12}\text{CO}(J=1-0)$ position-velocity diagrams of NGC3603. We see the two velocity components at 13 km s^{-1} and 28 km s^{-1} and a bridging feature in the velocity range $18 - 25 \text{ km s}^{-1}$ between the two clouds at $b = -0^{\circ}.6$ in Figure 6 a and at $l = 291^{\circ}.5 - 291^{\circ}.7$ in Figure 6 b.

Figures 7 and 8 show the distributions of the two clouds in $^{12}\text{CO}(J=2-1)$ overlaid on the infrared images in *JHK* bands, $8.3 \mu\text{m}$, and $25 \mu\text{m}$. For the blue-shifted cloud, we

see the molecular distribution is correlated with the cluster and the H II region. First, the cloud shows a depression toward the cluster at all CO lines, which suggests that the molecular gas toward the cluster has been dispersed by ionization/stellar winds. Second, the JHK distribution (Figure 7 b) shows that the northern peak of the blue-shifted cloud coincides with K band obscuration whose southeastern edge is delineated clearly at $(l, b = 291^{\circ}5 - 291^{\circ}65, -0^{\circ}5 - -0^{\circ}55)$ (Figures 7 c and d). Obscuration by the red-shifted cloud is too small to affect the near infrared image ($A_J, A_H, A_K = 0.1 - 0.7$ mag, see Table 2). It is unclear the cloud is in front or behind of the cluster, but we also see a hint of association between the cloud and the cluster/H II region; the cloud shows a similar depression toward the cluster, suggesting cloud dispersal due to the cluster.

3.2. Temperature and Density of the Molecular Clouds

In order to investigate the temperature of the molecular gas, which is a good indicator of physical association of the clouds with the cluster, we first examine the ratio of the CO($J=2-1$) and CO($J=1-0$) line intensities.

Figures 9 a and b show the distributions of the ratio of $J=2-1$ to $J=1-0$ line integrated intensities in ^{12}CO and ^{13}CO , for the blue-shifted cloud. The ^{12}CO distribution shows that the ratio is enhanced significantly near the cluster. We also see another enhancement of the ratio at the northern edge of the cloud. The high ratio of ^{12}CO (above 1.0) suggests high temperatures due to extra heating by high-mass stars, since the typical ratio is around 0.6 in clouds with no extra heat source (e.g., Sakamoto et al. 1997; Torii et al. 2011). We infer that the blue-shifted cloud as a whole is heated-up by the cluster. The heating is especially significant in the region within ~ 5 pc of the cluster, where the ratio is higher than 1.5. The ^{13}CO ratio is also enhanced to 1.0 – 2.7 within 10 pc of the cluster. We suggest that the irradiated surface layer of the cloud is better traced in the optically thick ^{12}CO than in the

optically thin ^{13}CO . The red-shifted cloud is not significantly detected in ^{13}CO and we show only the distribution of ^{12}CO ratio in Figure 9 c. The red-shifted cloud also shows enhanced ratios above 1.0 within a few pc of the cluster, suggesting the cloud is also heated-up by the cluster.

We chose here four positions for a detailed analysis of temperature and density. They are shown by letters A – D in Figure 9 and their coordinates are given in Table 3. The CO line profiles are shown in Figure 10. All four lines of ^{12}CO and ^{13}CO are detected in the four positions in the blue-shifted cloud, while only the two ^{12}CO lines are detected in the two positions in the red-shifted cloud.

In order to estimate the kinetic temperature and number density of the molecular clouds, we carried out an LVG analysis (Goldreich & Kwan 1974). The employed model assumes a spherically symmetric cloud where kinetic temperature T_{kin} , number density $n(\text{H}_2)$ and the radial velocity gradient dV/dr is taken to be uniform. We varied T_{kin} , and $n(\text{H}_2)$ within $T_{\text{kin}} = 6 - 500 \text{ K}$ and $n(\text{H}_2) = 10^2 - 10^6 \text{ cm}^{-3}$, where we fix $X(\text{CO})/(dv/dr) = 6.3 \times 10^{-5} (\text{km s}^{-1} \text{ pc}^{-1})^{-1}$. We assume $X(\text{CO}) = [^{12}\text{CO}]/[\text{H}_2] = 10^{-4}$ (e.g., Frerking et al. 1982; Leung et al. 1984) and a velocity gradient of $1.4 \text{ km s}^{-1} \text{ pc}^{-1}$. This value of dv/dr was derived by taking the average ratio between the cloud size and velocity width for the four clouds shown in Figure 10 (A–D). For the isotope ratio of $^{12}\text{C}/^{13}\text{C}$, we adopt 75 at the Galactocentric distance of $\sim 9 \text{ kpc}$ (Milam et al. 2005). We derived T_{kin} and $n(\text{H}_2)$ in the four positions of the blue-shifted cloud. We used the line intensity ratios of the $^{12}\text{CO}(J=2-1)$, $^{13}\text{CO}(J=2-1)$ and $^{13}\text{CO}(J=1-0)$ transitions. The $^{12}\text{CO}(J=1-0)$ line was not used here because the line may be optically thick and sample mainly the surface layer the cloud. Figure 11 shows the results and the derived values are listed in Table 3. The temperature is significantly enhanced with respect to quiescent molecular cloud temperatures, falling in the range $30 - 50 \text{ K}$ in the blue-shifted cloud for a

density of $3 - 5 \times 10^3 \text{ cm}^{-3}$, confirming significant heating by the cluster.

We then estimate the temperature range of the red-shifted cloud from the line intensity ratio of $^{12}\text{CO}(J=2-1)$ to $^{12}\text{CO}(J=1-0)$. Figure 12 shows the ratio as a function of density and temperature, where the line intensity is calculated by the LVG approximation. The molecular column density at positions A and C is estimated from the $^{12}\text{CO}(J=1-0)$ integrated intensity by using an empirical X-factor of $2.0 \times 10^{20} \text{ cm}^{-2} (\text{K km s}^{-1})^{-1}$. By assuming the width of the cloud to be $\sim 1 \text{ pc}$ from the $\text{CO}(J=2-1)$ distribution, we estimate that the density is lower than $\sim 10^3 \text{ cm}^{-3}$ and that the secure lower limit for temperature is estimated to be higher than 20 K for the 3σ error limit in Figure 12. This indicates that the red-shifted cloud is also heated-up by the cluster NGC3603, the only known strong heat source toward the direction.

Based on the analysis above, we conclude that the two clouds are located within $\sim 10 \text{ pc}$ of the cluster and adopt 7 kpc as the distance, the same value as that of the cluster, instead of their kinematic distances of 8 – 9 kpc. For this distance the cloud masses are estimated to be $7.2 \times 10^4 M_{\odot}$ and $1.2 \times 10^4 M_{\odot}$ for the blue-shifted cloud and the red-shifted cloud, respectively (Table 4).

4. DISCUSSION

Previous work has shown that the 13 km s^{-1} molecular cloud is physically linked to the super star cluster NGC3603 as shown by the PDR irradiated by the cluster (Röllig et al. 2011). The present observations confirm this, and also show that there is another extended molecular cloud at 28 km s^{-1} toward NGC3603. We suggest that the 13 km s^{-1} molecular cloud (blue-shifted cloud) and the 28 km s^{-1} molecular cloud (red-shifted cloud) are both physically associated with NGC3603. The association is verified by the high temperature of

the molecular clouds toward the cluster as derived from an analysis of multi CO transitions, and is consistent with the morphological correlation between CO and NGC3603. This is a similar situation to the two molecular clouds associated with the super star cluster Westerlund2/RCW49. For Westerlund2 it is suggested that a collision between the two clouds triggered formation of the cluster, where the relative velocity is ascribed to the original bulk motion of the clouds (Paper I; Ohama et al. 2010), and it is possible that a similar collisional process is also working in NGC3603.

By considering possible projection effects, the observed line-of-sight velocity separation gives a lower limit for the actual relative velocity. If we assume random cloud motions primarily restricted to the Galactic plane and adopt $\sqrt{2} \times 15 \sim 20 \text{ km s}^{-1}$ as the relative velocity, the total mass required to gravitationally bind the two clouds is $10^6 M_{\odot}$ within 10 pc of the cluster. It is one order of magnitude larger than the total mass inside the system $\sim 10^5 M_{\odot}$. We examine an idea that the cloud velocity separation is due to feedback from the cluster or nearby objects. Supernova remnants (SNRs) may be a possible source of the kinetic energy. There are two SNRs toward the region, SNR G292.5–0.1 (Whiteoak & Green 1996) and SNR G292.5–0.5 (Crawford et al. 2001) with a pulsar PSR J1119–6127 (Gonzalez et al. 2007; Safi-Harb & Kumar 2008). These are, however, separated from NGC3603 by 0.5 degrees and are not likely to be affecting the molecular clouds. It is also possible that SNRs older than 10^4 yr nearby may have affected the cloud motion via SN shock waves in the last Myrs. If they were influential, one may expect curved velocity field in the two GMCs which may last over Myrs. The velocity distributions of the present two GMCs however show fairly uniform peak velocity distribution, suggesting such stellar acceleration was not influential.

The velocity difference is not likely due to the stellar-wind acceleration, either. It is noted that the stellar winds in NGC3603 are affecting an area only within 1 pc of the

cluster (Balick et al. 1980; Clayton 1986, 1990), while the H II region ionized by the cluster is extended within a 10 pc radius (Clayton 1986, 1990). The red-shifted cloud is extended far beyond 10 pc with no large velocity shift in the order of 10 km s^{-1} , indicating that the cloud is not strongly affected by the stellar winds, while a small velocity red-shift of $\sim 2 \text{ km s}^{-1}$ toward the cluster within 10 pc in the red-shifted cloud (Figure 6) may possibly be ascribed to the stellar-wind acceleration. The kinetic energy of this shift is estimated to be $\sim 3 \times 10^{47} \text{ erg}$, and can be supplied by the stellar winds having kinetic energy $\sim 5 \times 10^{51} \text{ erg}$ for a 1 Myr timescale of the highest mass O stars (Harayama et al. 2008), which are most effective in the stellar winds (Drissen et al. 1995). If the velocity separation between the two clouds are mainly due to the stellar winds, the velocity separation of the compact blue-shifted cloud 20 km s^{-1} might be ascribed to such acceleration. The kinetic energy of the blue-shifted cloud relative to the red-shifted cloud is $\sim 1.6 \times 10^{50} \text{ erg}$ for the cloud mass $8.4 \times 10^4 M_{\odot}$ and the relative velocity 20 km s^{-1} . This energy corresponds to several percent of the stellar wind energy, and the acceleration can be possible if the energy requirement alone is considered. A serious difficulty here, however, is that the blue-shifted cloud shows no such a trend that the velocity separation from the red-shifted cloud becomes large toward the cluster at a pc scale. The cluster is apparently located on the axis of the cloud elongation in the north to south, and the cloud geometry suggests that most of the cloud cannot be exposed to the winds from cluster. This is a quite unfavorable configuration for the cloud to be accelerated. Remembering that the stellar winds are affecting only 1 pc radius (Balick et al. 1980; Clayton 1986, 1990), we conclude it highly unlikely that the blue-shifted cloud as a whole was accelerated by the stellar winds of NGC3603.

We consider that the association of the two clouds is by chance, and that they were moving independently before their encounter. The relative velocity 20 km s^{-1} is likely due to random motion of the clouds. We here present a scenario that a cloud-cloud collision between the two clouds triggered the formation of NGC3603. The bridging feature discussed

in Section 3.1 suggests that the two clouds are physically interacting; numerical simulations of cloud-cloud collisions find the intermediate velocity features between the two colliding clouds (Habe & Ohta 1992; Anathpindika 2010; Anathpindika & Bhatt 2012). In these models two colliding clouds form a compressed layer which is highly turbulent and dense, leading to the formation of dense clumps where high-mass stars are formed. NGC3603 is the second case of such collision-induced formation of a super star cluster along side Westerlund 2, if the scenario is correct. In NGC3603, we infer that the collision took place ~ 1 Myrs ago as estimated by the ratio of the cloud size 20 pc and the velocity separation 20 km s^{-1} . This is obviously an order-of-magnitude estimate at best and the value may be different by a factor of ~ 2 due to projection effects in space and velocity. It is however quite unnatural that the time scale can be different by a factor of ten. The blue-shifted cloud is located on the near side of NGC3603 (*JHK* in Figure 7 b), which is consistent with a collision that occurred in the past. A similar argument is given in M20 (Torii et al. 2011). The blue-shifted cloud has a molecular mass of $7.2 \times 10^4 M_\odot$ and the red-shifted cloud $1.2 \times 10^4 M_\odot$ within a radius of 20 pc from the cluster. Both clouds show intensity depressions toward the cluster within a radius of several pc, which includes about ten highest-mass stars having $\sim 100 M_\odot$ in the cluster core within a radius of 1 pc (Stolte et al. 2004; Sung & Bessell 2004; Harayama et al. 2008). From these the dissipated cloud mass is roughly estimated to be on the order of $10^4 M_\odot$ consistent with the mass and the age of the highest-mass members of the cluster core $\sim 10^4 M_\odot$ and ~ 1 Myr (Stolte et al. 2004; Sung & Bessell 2004; Harayama et al. 2008) for a star formation efficiency of $\sim 10\%$. We suggest that the molecular mass compressed by the collision is around $10^4 M_\odot$, which corresponds to the mass of a cloud with a molecular column density of 10^{23} cm^{-2} for a radius of 1.5 pc. The highest molecular column density observed is $6 \times 10^{22} \text{ cm}^{-2}$ toward the northern peak of the blue-shifted cloud, supporting the assumption of such a high column density as the initial condition prior to the collision.

The higher-mass stars above $20 M_{\odot}$ have a different slope from that of the lower-mass stars in the mass function in NGC3603 (Harayama et al. 2008). It is possible that stars of less than $20 M_{\odot}$ may have large ages more than several Myrs and may have been already formed prior to the collision. Recent studies show some low-mass cluster members obviously older than 3 Myr (e.g., Kudryavtseva et al. 2012; Pang et al. 2013), which could be an evidence for the earlier star formation. The formation of high-mass stars can take place on the order of 10^5 yrs at a very high mass accretion rate of $10^{-3} M_{\odot} \text{ yr}^{-1}$ as theoretically suggested (Tan & McKee 2002). This high mass accretion rate is sustainable by the increased turbulence in the shocked layer created by the supersonic collision (Anathpindika 2010; Inoue et al. 2013). Another issue is the mass segregation of higher-mass stars toward the cluster (e.g., Sung & Bessell 2004); it has been a puzzle how the mass segregation of the higher-mass stars takes place in rich clusters including NGC3603 because gravitational segregation is a long-term process which takes over 10 Myrs (Zinnecker & Yorke 2007; Harayama et al. 2008). Cloud-cloud collisions have the potential to cause such mass segregation at the spot of the collisional interaction where molecular density distribution is peaked prior to the collision.

In NGC3603 recent observations indicates that the age spread of the member stars is very short, less than 0.1 Myrs (Kudryavtseva et al. 2012). This spread is significantly shorter than the sound travel time 1 – 10 Myrs for a sound speed of $0.1 - 1 \text{ km s}^{-1}$. It is notable that the cloud-cloud collision at a high speed of 20 km s^{-1} provides a reasonable explanation for this very short age spread. In addition, the velocities of the recombination lines and OH absorption lines measured for the nebula surrounding NGC3603 are $8 - 14 \text{ km s}^{-1}$ in V_{LSR} (Moffat & Niemela 1984, and references therein), similar to that of the blue-shifted cloud, having the larger molecular column density than the red shifted cloud. This is consistent with that the cloud as the parent of the cluster.

The present study has shown that the super star cluster NGC3603 may be the a second super star cluster formed by triggering due to a cloud-cloud collision, along side the super star cluster Westerlund 2. This suggests that the rare rich star clusters are formed preferentially in the dense interface layer created between two colliding clouds. As mentioned in Section 1, there are only four super star clusters in the Galaxy that show nebulosity, a hint of the parent cloud(s) of the clusters, but the remainder has no such nebulosity, indicating that their parent clouds are fully dissipated via ionization etc. It is important to make molecular observations of the other two with associated nebulosity to test if they are also formed by cloud-cloud collisions.

The frequent occurrence of cloud-cloud collisions has been suggested by global numerical simulations of a galactic disk (Tasker & Tan 2009) and recent observations suggest the importance of cloud-cloud collisions in triggering star formation. Some authors have reported the collision between smaller molecular clouds with $100 - 1000 M_{\odot}$. For instance, Torii et al. (2011) presented CO($J=2-1$) and CO($J=1-0$) observations of M20 with NANTEN2 and argued that a first generation O-type star (Walborn 1973; Chaisson & Willson 1975) was formed by a cloud-cloud collision on the order of 0.5 Myrs or less. Also triggered formation is suggested in NGC1333 (Loren 1976), Sgr B2 (Hasegawa et al. 1994; Sato et al. 2000), W49N (Buckley & Ward-Thompson 1996; Miyawaki et al. 2009), IRAS 0400+5025 (Xue & Wu 2008), W51 (Kang et al. 2010), S87, S88B, AFGL5142, AFGL5180 (Higuchi et al. 2010), Serpens north (Duarte-Cabral et al. 2010), the stellar cluster L1641-N (Nakamura et al. 2012) and in a further 201 candidates identified from cold IRAS sources (Li & Wang 2012). We note that some of these observational results only present circumstantial evidence. The cloud-cloud collision is not a unique interpretation of these observations, because the relatively small velocity separations observed allow the clouds/clumps to be gravitationally bound. The colliding clouds in the two SSCs, NGC3603 and Westerlund 2, Sgr B2 and M20 have large velocity

separations of $8 - 30 \text{ km s}^{-1}$ and they are not gravitationally bound by the observed cloud mass. The argument on gravitational binding is crucial in order to verify the cloud-cloud collision by excluding gravitationally bound motions. In order to better understand the role of cloud-cloud collisions in triggering star formation, it is required to have a larger sample of cloud-cloud collisions identified from gravitationally unbound systems.

5. SUMMARY

The conclusions of the present work are given as follows;

1) We have found two molecular clouds at around 13 km s^{-1} and 28 km s^{-1} toward NGC3603 and have shown both are physically associated with NGC3603. This association is verified by the higher temperature of the molecular gas toward the H II region as indicated by enhanced $\text{CO}(J=2-1/1-0)$ intensity ratios, and is consistent with the morphological correspondence between the molecular gas and the H II region and also with a bridging feature in velocity between the two clouds.

2) The velocity separation of the two clouds, 20 km s^{-1} , indicates that the two are not gravitationally bound. Expansion driven by stellar winds also does not provide a good explanation for the cloud motions either. The physical association of the two clouds therefore must be due to an accidental encounter between them. We suggest that the two clouds collided with each other $\sim 1 \text{ Myrs}$ ago and this collision triggered the formation of the super star cluster NGC3603 via the strong compression of dense molecular gas in the shocked layer.

3) The formation of the super star cluster is very rapid within $\sim 1 \text{ Myr}$ as estimated from the collision timescale and this is consistent with the theory of rapid high-mass star formation by high-mass accretion rate. The large mass accretion rate is likely sustained by

the large turbulence excited by the shock interaction. This is the second case of formation of a super star cluster by triggering in a cloud-cloud collision along side Westerlund2

NANTEN2 is an international collaboration of ten universities, Nagoya University, Osaka Prefecture University, University of Cologne, University of Bonn, Seoul National University, University of Chile, University of New South Wales, Macquarie University, University of Sydney and Zurich Technical University. The work is financially supported by a Grant-in-Aid for Scientific Research (KAKENHI, Nos. 15071203, 21253003, and 20244014) from MEXT (the Ministry of Education, Culture, Sports, Science and Technology of Japan) and JSPS (Japan Society for the Promotion of Science) as well as JSPS core-to-core program (No. 17004). We also acknowledge the support of the Mitsubishi Foundation and the Sumitomo Foundation. This research was supported by the Grant-in-Aid for Nagoya University Global COE Program, “Quest for Fundamental Principles in the Universe: from Particles to the Solar System and the Cosmos”, from MEXT. Also, the work makes use of archive data acquired with *Spitzer Space Telescope* and IRAS data gained with Infrared Processing and Analysis Center (IPAC). *Spitzer* is controlled by the Jet Propulsion Laboratory, California Institute of Technology under a contract with NASA.

REFERENCES

- Anathpindika, S., & Bhatt, H. C. 2012, MNRAS, 427, 1713
- Anathpindika, S. V. 2010, MNRAS, 405, 1431
- Ascenso, J., Alves, J., Vicente, S., & Lago, M. T. V. T. 2007, VizieR Online Data Catalog, 347, 60199
- Balick, B., Boeshaar, G. O., & Gull, T. R. 1980, ApJ, 242, 584
- Bohlin, R. C., Savage, B. D., & Drake, J. F. 1978, ApJ, 224, 132
- Bonnell, I. A., Bate, M. R., & Zinnecker, H. 1998, MNRAS, 298, 93
- Brandl, B., Brandner, W., Eisenhauer, F., et al. 1999, A&A, 352, L69
- Brandner, W., Grebel, E. K., Chu, Y.-H., et al. 2000, AJ, 119, 292
- Buckley, H. D., & Ward-Thompson, D. 1996, MNRAS, 281, 294
- Cardelli, J. A., Clayton, G. C., & Mathis, J. S. 1989, ApJ, 345, 245
- Caswell, J. L., & Haynes, R. F. 1987, A&A, 171, 261
- Chaisson, E. J., & Willson, R. F. 1975, ApJ, 199, 647
- Clark, J. S., Negueruela, I., Crowther, P. A., & Goodwin, S. P. 2005, A&A, 434, 949
- Clark, J. S., Ritchie, B. W., & Negueruela, I. 2010, A&A, 514, A87
- Clayton, C. A. 1986, MNRAS, 219, 895
- . 1990, MNRAS, 246, 712
- Crawford, F., Gaensler, B. M., Kaspi, V. M., et al. 2001, ApJ, 554, 152

- Crowther, P. A., & Dessart, L. 1998, MNRAS, 296, 622
- Cutri, R. M., Skrutskie, M. F., van Dyk, S., et al. 2003, VizieR Online Data Catalog, 2246, 0
- de Pree, C. G., Nysewander, M. C., & Goss, W. M. 1999, AJ, 117, 2902
- Drissen, L., Moffat, A. F. J., Walborn, N. R., & Shara, M. M. 1995, AJ, 110, 2235
- Duarte-Cabral, A., Fuller, G. A., Peretto, N., et al. 2010, A&A, 519, A27
- Elmegreen, B. G. 1998, in Astronomical Society of the Pacific Conference Series, Vol. 148, Origins, ed. C. E. Woodward, J. M. Shull, & H. A. Thronson, Jr., 150
- Elmegreen, B. G., & Lada, C. J. 1977, ApJ, 214, 725
- Figer, D. F., Kim, S. S., Morris, M., et al. 1999, ApJ, 525, 750
- Franco, J., Shore, S. N., & Tenorio-Tagle, G. 1994, ApJ, 436, 795
- Frerking, M. A., Langer, W. D., & Wilson, R. W. 1982, ApJ, 262, 590
- Furukawa, N., Dawson, J. R., Ohama, A., et al. 2009a, ApJ, 696, L115
- . 2009b, ApJ, 696, L115
- Goldreich, P., & Kwan, J. 1974, ApJ, 189, 441
- Gonzalez, M. E., Kaspi, V. M., Camilo, F., Gaensler, B. M., & Pivovarovoff, M. J. 2007, Ap&SS, 308, 89
- Goss, W. M., & Radhakrishnan, V. 1969, Astrophys. Lett., 4, 199
- Grabelsky, D. A., Cohen, R. S., Bronfman, L., & Thaddeus, P. 1988, ApJ, 331, 181
- Habe, A., & Ohta, K. 1992, PASJ, 44, 203

- Harayama, Y., Eisenhauer, F., & Martins, F. 2008, *ApJ*, 675, 1319
- Hasegawa, T., Sato, F., Whiteoak, J. B., & Miyawaki, R. 1994, *ApJ*, 429, L77
- Higuchi, A. E., Kuroono, Y., Saito, M., & Kawabe, R. 2010, *ApJ*, 719, 1813
- Hofmann, K.-H., Seggewiss, W., & Weigelt, G. 1995, *A&A*, 300, 403
- Hosokawa, T., & Inutsuka, S.-i. 2006, *ApJ*, 648, L131
- Hunter, D. A., Boyd, D. M., & Hawley, W. N. 1995a, *ApJS*, 99, 551
- Hunter, D. A., Shaya, E. J., Scowen, P., et al. 1995b, *ApJ*, 444, 758
- Inoue, R., Tanaka, S.-I.-R., Namiki, R., Sagawa, T., & Takahashi, Y. 2013, ArXiv e-prints, arXiv:1301.1016
- Johnson, K. E. 2005, in *IAU Symposium*, Vol. 227, *Massive Star Birth: A Crossroads of Astrophysics*, ed. R. Cesaroni, M. Felli, E. Churchwell, & M. Walmsley, 413–422
- Kang, M., Bieging, J. H., Kulesa, C. A., et al. 2010, *ApJS*, 190, 58
- Kennicutt, Jr., R. C. 1984, *ApJ*, 287, 116
- Kudryavtseva, N., Brandner, W., Gennaro, M., et al. 2012, *ApJ*, 750, L44
- Leung, C. M., Herbst, E., & Huebner, W. F. 1984, *ApJS*, 56, 231
- Li, N., & Wang, J.-J. 2012, ArXiv e-prints, arXiv:1212.0084
- Loren, R. B. 1976, *ApJ*, 209, 466
- Maíz-Apellániz, J., Pérez, E., & Mas-Hesse, J. M. 2004, *AJ*, 128, 1196
- Massey, P., & Hunter, D. A. 1998, *ApJ*, 493, 180

- Melnick, J., Tapia, M., & Terlevich, R. 1989, *A&A*, 213, 89
- Milam, S. N., Savage, C., Brewster, M. A., Ziurys, L. M., & Wyckoff, S. 2005, *ApJ*, 634, 1126
- Miyawaki, R., Hayashi, M., & Hasegawa, T. 2009, *PASJ*, 61, 39
- Mizuno, A., & Fukui, Y. 2004, in *Astronomical Society of the Pacific Conference Series*, Vol. 317, *Milky Way Surveys: The Structure and Evolution of our Galaxy*, ed. D. Clemens, R. Shah, & T. Brainerd, 59
- Mizutani, K., Suto, H., Takami, H., et al. 1987, *MNRAS*, 228, 721
- Moffat, A. F. J. 1974, *A&A*, 35, 315
- . 1983, *A&A*, 124, 273
- Moffat, A. F. J., & Niemela, V. S. 1984, *ApJ*, 284, 631
- Moffat, A. F. J., Poitras, V., Marchenko, S. V., et al. 2004, *AJ*, 128, 2854
- Nakajima, T., Kaiden, M., Korogi, J., et al. 2007, *PASJ*, 59, 1005
- Nakamura, F., Miura, T., Kitamura, Y., et al. 2012, *ApJ*, 746, 25
- Nürnberg, D. E. A., Bronfman, L., Yorke, H. W., & Zinnecker, H. 2002, *A&A*, 394, 253
- Ohama, A., Dawson, J. R., Furukawa, N., et al. 2010, *ApJ*, 709, 975
- Pandey, A. K., Ogura, K., & Sekiguchi, K. 2000, *PASJ*, 52, 847
- Pang, X., Grebel, E. K., Allison, R. J., et al. 2013, *ApJ*, 764, 73
- Pfalzner, S. 2009, *A&A*, 498, L37
- Portegies Zwart, S. F., McMillan, S. L. W., & Gieles, M. 2010, *ARA&A*, 48, 431

- Rochau, B., Brandner, W., Stolte, A., et al. 2010, *ApJ*, 716, L90
- Röllig, M., Kramer, C., Rajbahak, C., et al. 2011, *A&A*, 525, A8
- Safi-Harb, S., & Kumar, H. S. 2008, *ApJ*, 684, 532
- Sakamoto, S., Hasegawa, T., Handa, T., Hayashi, M., & Oka, T. 1997, *ApJ*, 486, 276
- Sato, F., Hasegawa, T., Whiteoak, J. B., & Miyawaki, R. 2000, *ApJ*, 535, 857
- Schmutz, W., & Drissen, L. 1999, in *Revista Mexicana de Astronomia y Astrofisica*, vol. 27, Vol. 8, *Revista Mexicana de Astronomia y Astrofisica Conference Series*, ed. N. I. Morrell, V. S. Niemela, & R. H. Barbá, 41–48
- Schneider, N., Stutzki, J., Winnewisser, G., & Block, D. 1998, *A&A*, 335, 1049
- Stolte, A., Brandner, W., Brandl, B., Zinnecker, H., & Grebel, E. K. 2004, *AJ*, 128, 765
- Sung, H., & Bessell, M. S. 2004, *AJ*, 127, 1014
- Tan, J. C., & McKee, C. F. 2002, in *Astronomical Society of the Pacific Conference Series*, Vol. 267, *Hot Star Workshop III: The Earliest Phases of Massive Star Birth*, ed. P. Crowther, 267
- Tan, J. C., & McKee, C. F. 2004, *ApJ*, 603, 383
- Tasker, E. J., & Tan, J. C. 2009, *ApJ*, 700, 358
- Torii, K., Enokiya, R., Sano, H., et al. 2011, *ApJ*, 738, 46
- van den Bergh, S. 1978, *A&A*, 63, 275
- Walborn, N. R. 1973, *ApJ*, 182, L21
- Wang, J., & Chen, Y. 2010, *Science in China G: Physics and Astronomy*, 53, 271

Whiteoak, J. B. Z., & Green, A. J. 1996, A&AS, 118, 329

Whitworth, A. 1979, MNRAS, 186, 59

Wilson, C. D., Scoville, N., Madden, S. C., & Charmandaris, V. 2000, ApJ, 542, 120

Xue, R., & Wu, Y. 2008, ApJ, 680, 446

Zinnecker, H., & Yorke, H. W. 2007, ARA&A, 45, 481

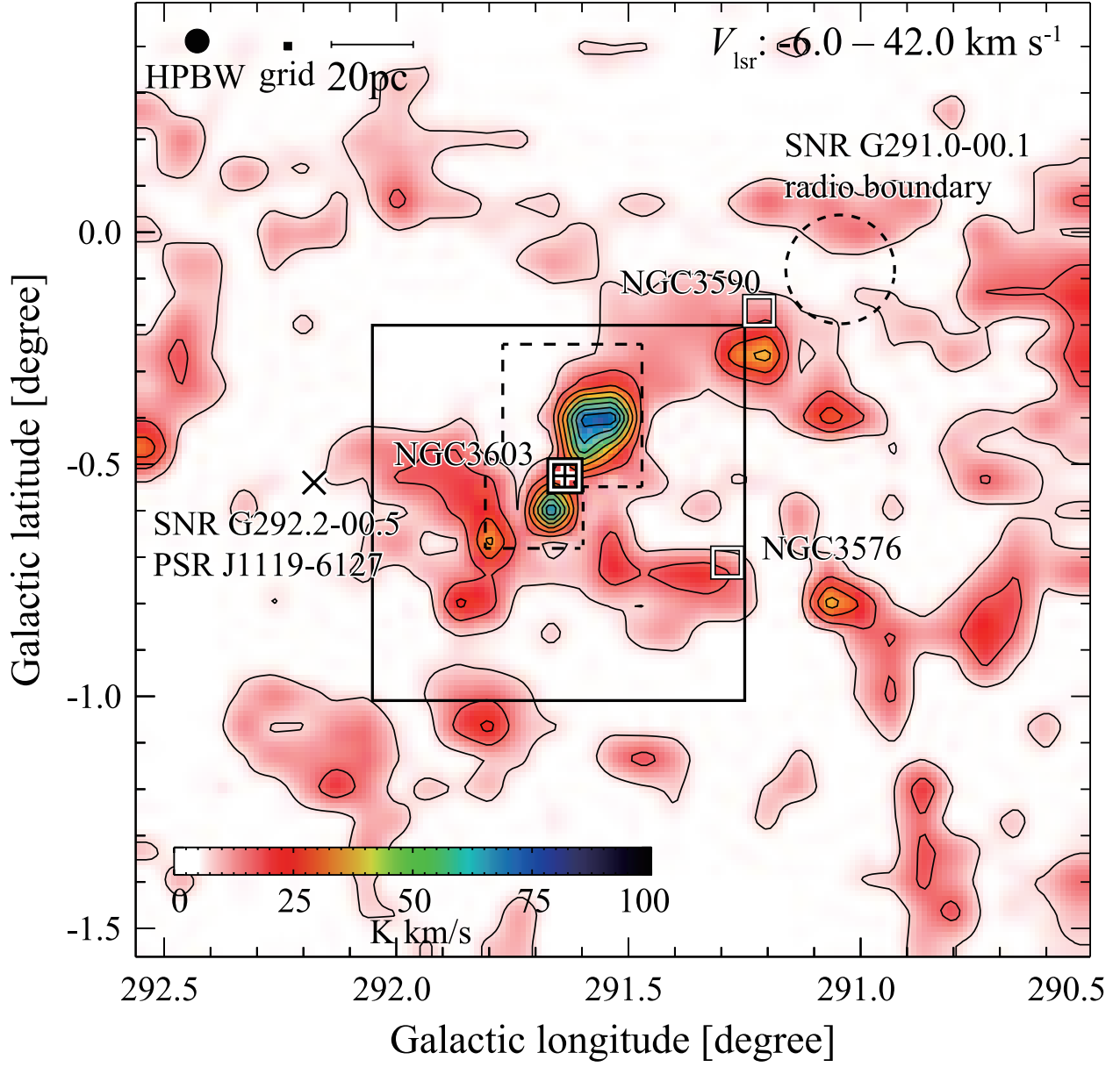


Fig. 1.— Integrated intensity distribution of NANTEN2 $^{12}\text{CO}(J=1-0)$ emission toward $(l, b) = (290^\circ.5 - 292^\circ.5, -1^\circ.5 - 0^\circ.5)$. Contours are drawn every 10 K km s^{-1} from 5 K km s^{-1} . The square indicates NGC 3603, and solid lines indicate the region shown in Figures 2 – 5. The dashed lines show the region observed in $^{13}\text{CO}(J=2-1)$.

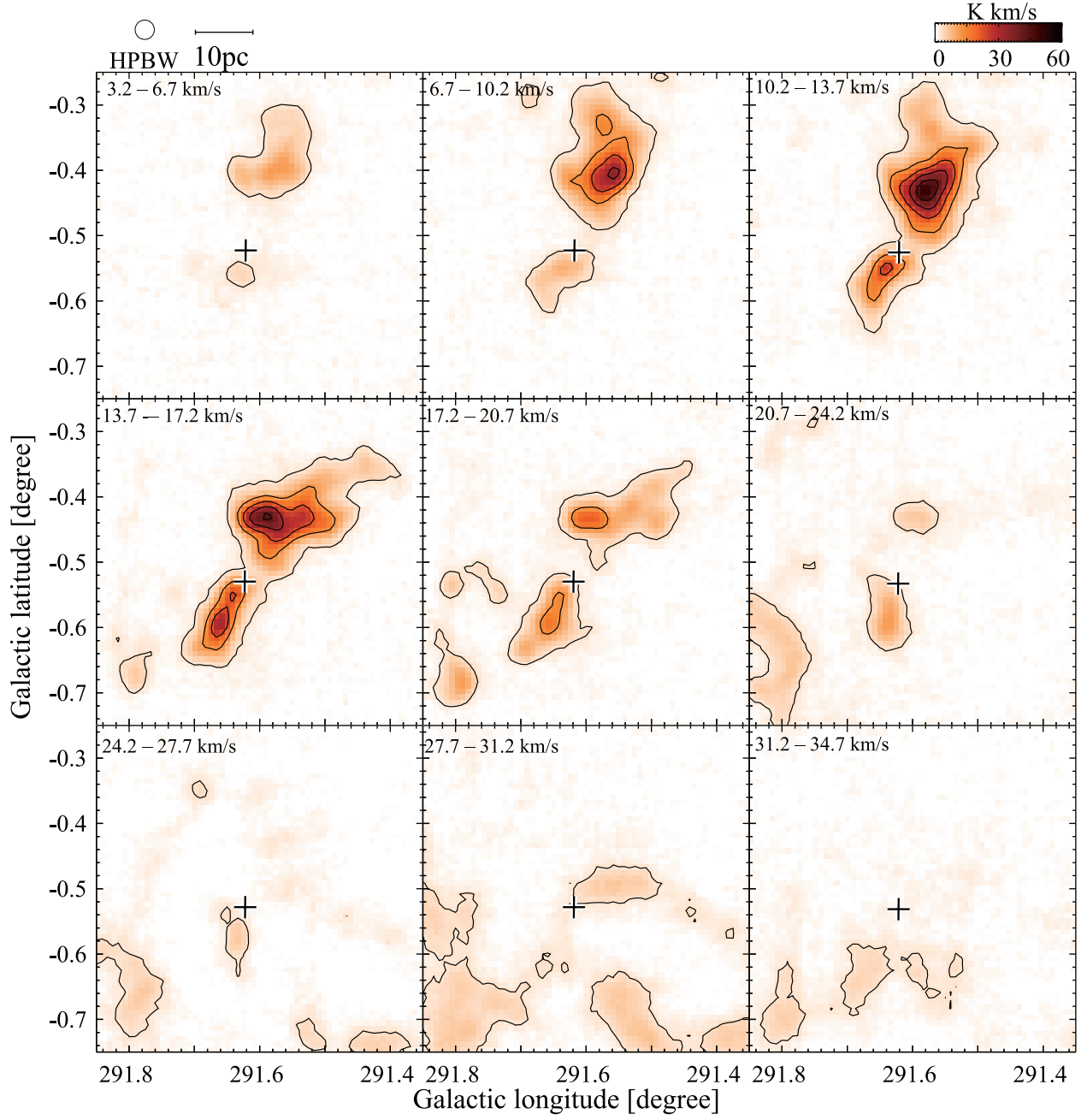


Fig. 2.— Velocity channel maps of $^{12}\text{CO}(J=2-1)$ intensity integrated over 3.5 km s^{-1} bins. Contours are drawn every 6.0 K km s^{-1} from 2.4 K km s^{-1} . The cross corresponds to the position of the cluster NGC3603.

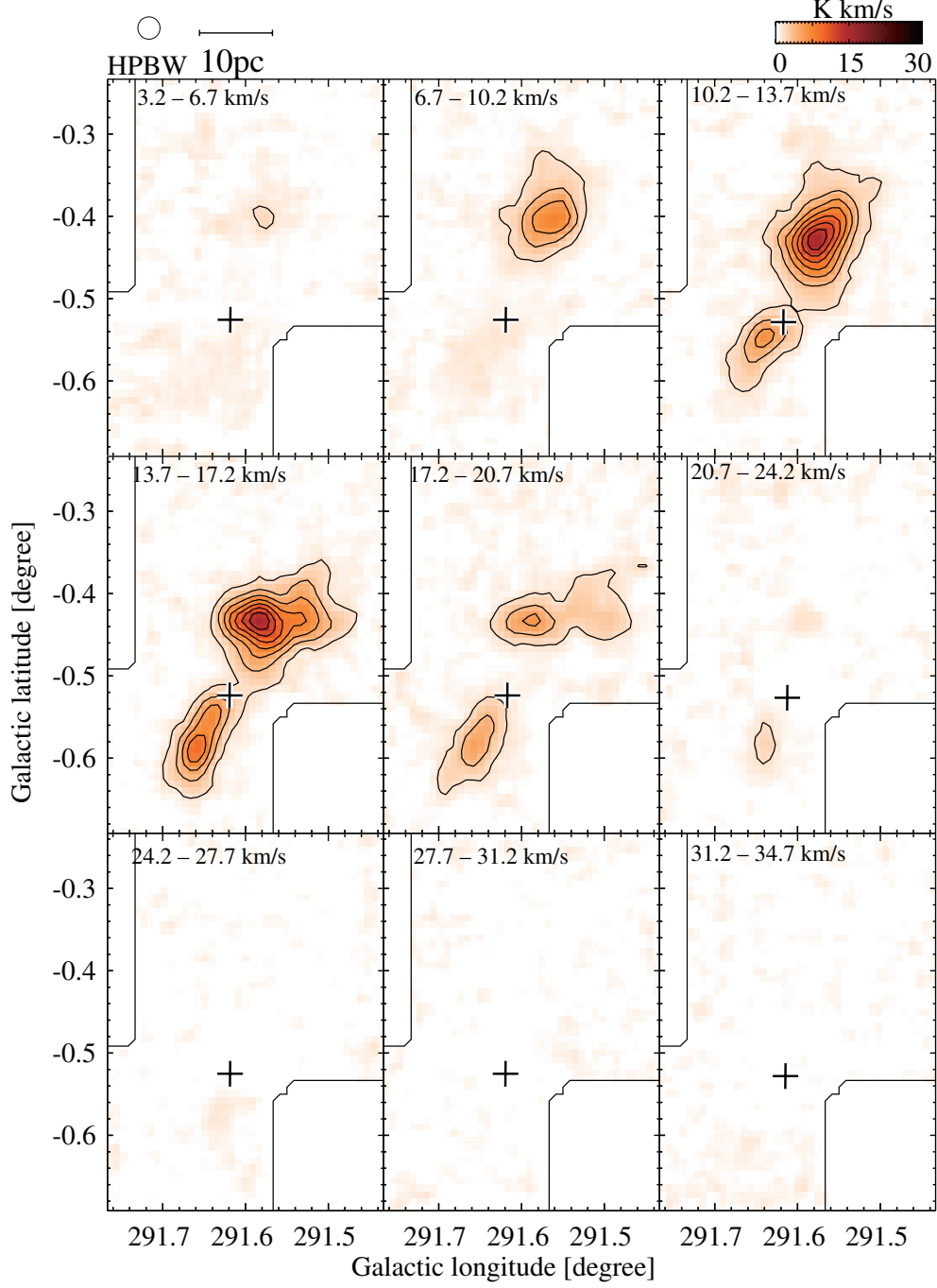


Fig. 3.— Velocity channel maps of $^{13}\text{CO}(J=2-1)$ intensity integrated over 3.5 km s^{-1} bins. Contours are drawn every 2.0 K km s^{-1} from 1.3 K km s^{-1} . The cross corresponds to the position of the cluster NGC3603.

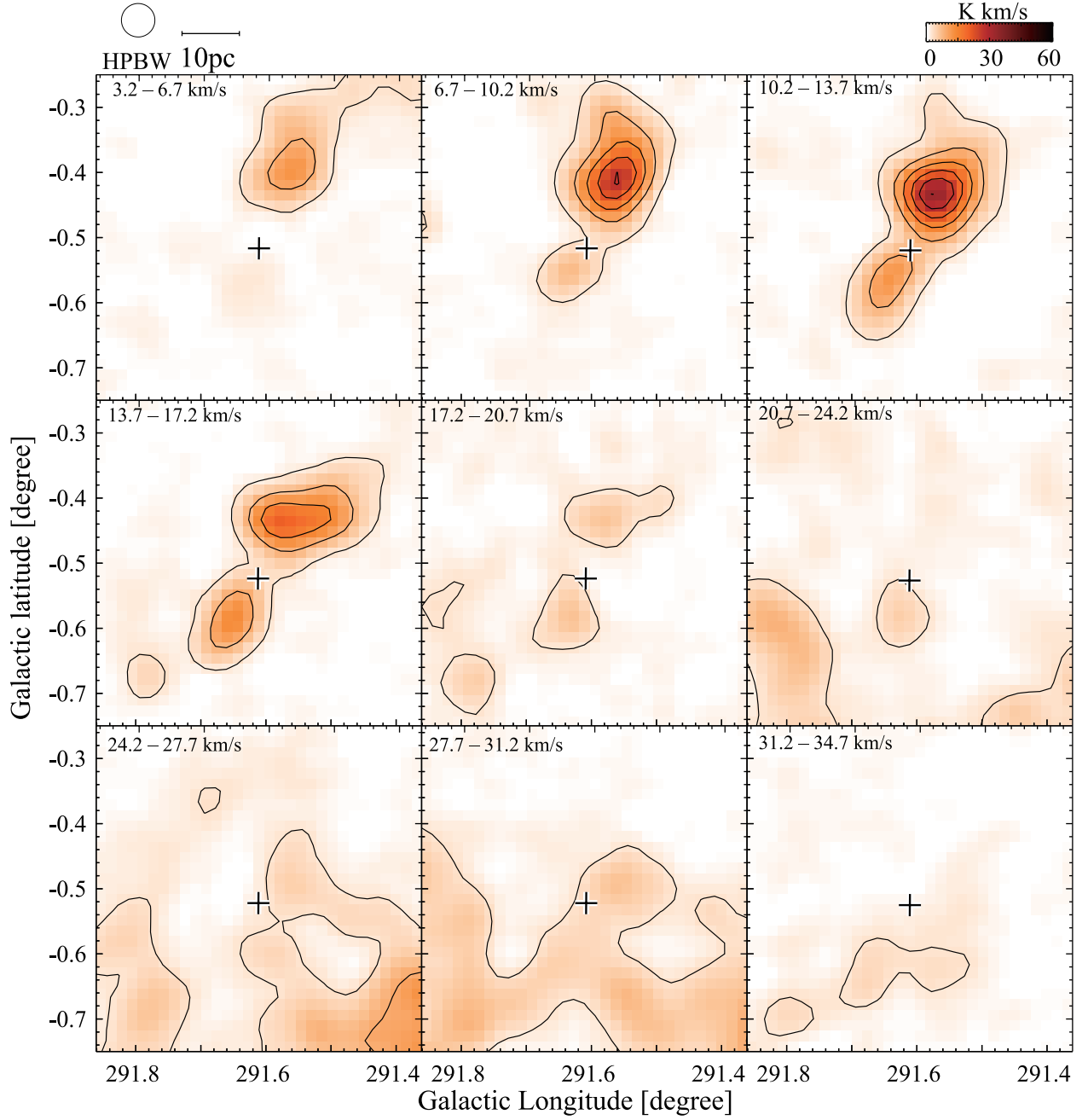


Fig. 4.— Velocity channel maps of $^{12}\text{CO}(J=1-0)$ intensity integrated over 3.5 km s^{-1} bins. Contours are drawn every 6.0 K km s^{-1} from 2.4 K km s^{-1} . The cross corresponds to the position of the cluster NGC3603.

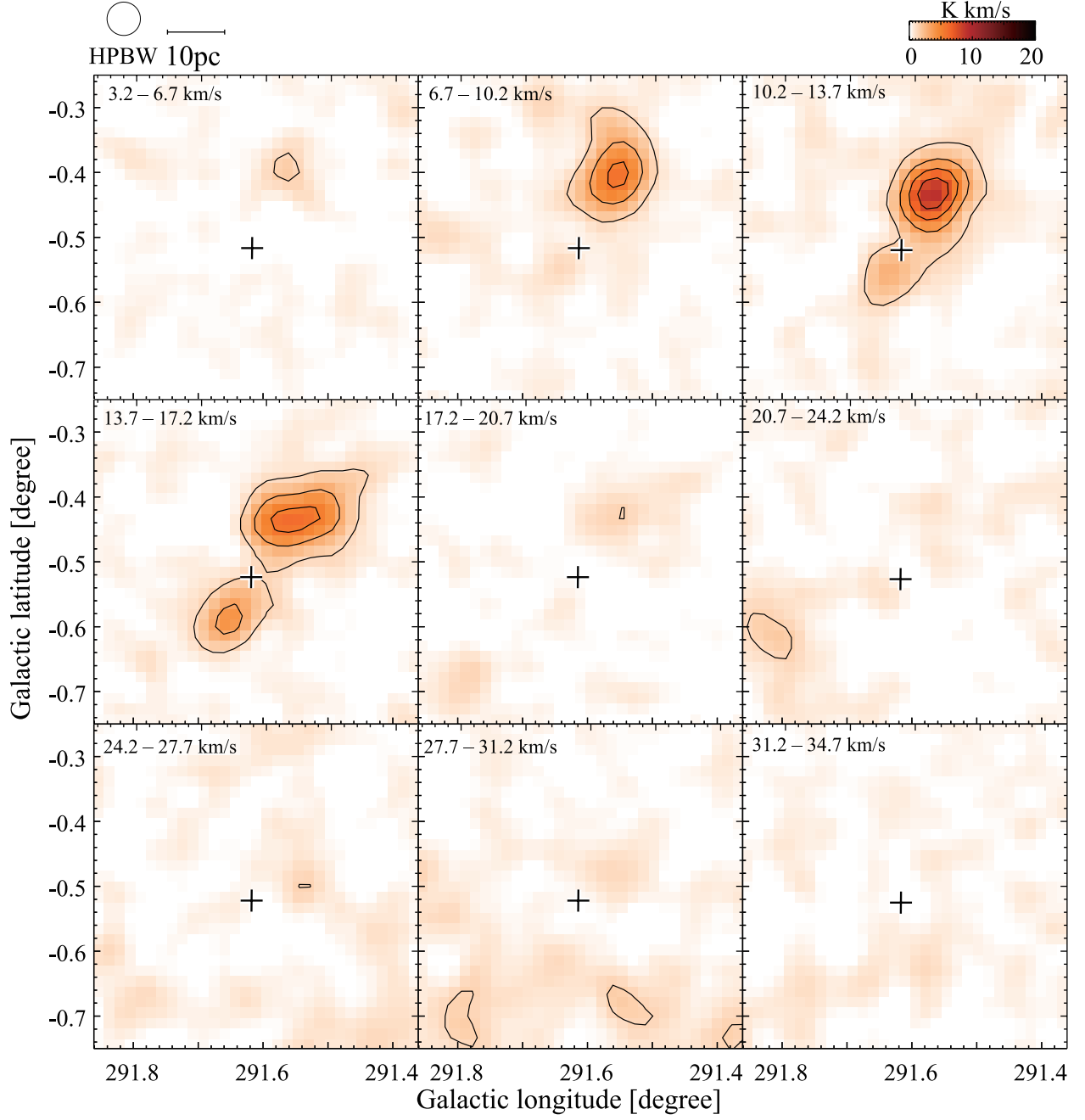


Fig. 5.— Velocity channel maps of $^{13}\text{CO}(J=1-0)$ intensity integrated over 3.5 km s^{-1} bins. Contours are drawn every 2.0 K km s^{-1} from 1.4 K km s^{-1} . The cross corresponds to the position of the cluster NGC3603.

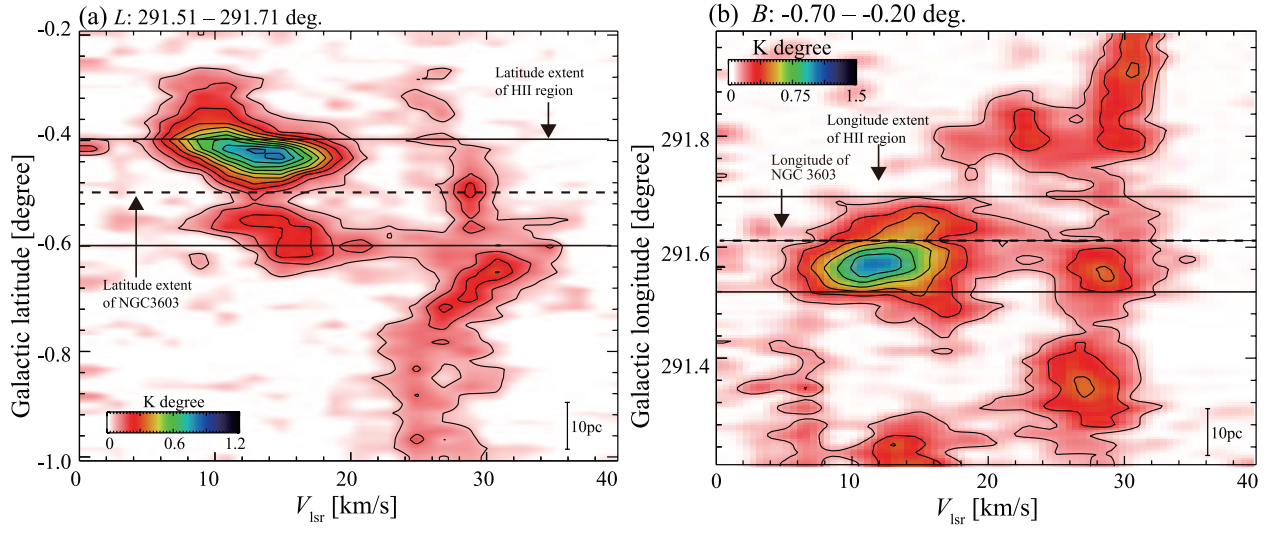


Fig. 6.— (a) Velocity vs. galactic latitude diagram for $^{12}\text{CO}(J=1-0)$ emission integrated over a longitude range of $291^\circ 51 - 291^\circ 71$. Contours are plotted every 0.06 K degree from 0.02 K degree. The solid lines depict the extent of the H II region observed by the *Spitzer Space Telescope*. The dashed line depicts the latitude position of NGC3603. (b) Velocity vs. galactic longitude diagram for $^{12}\text{CO}(J=1-0)$ emission integrated over a latitude range of $-0^\circ 70 - -0^\circ 20$. Contours are plotted every 0.15 K degree from 0.15 K degree.

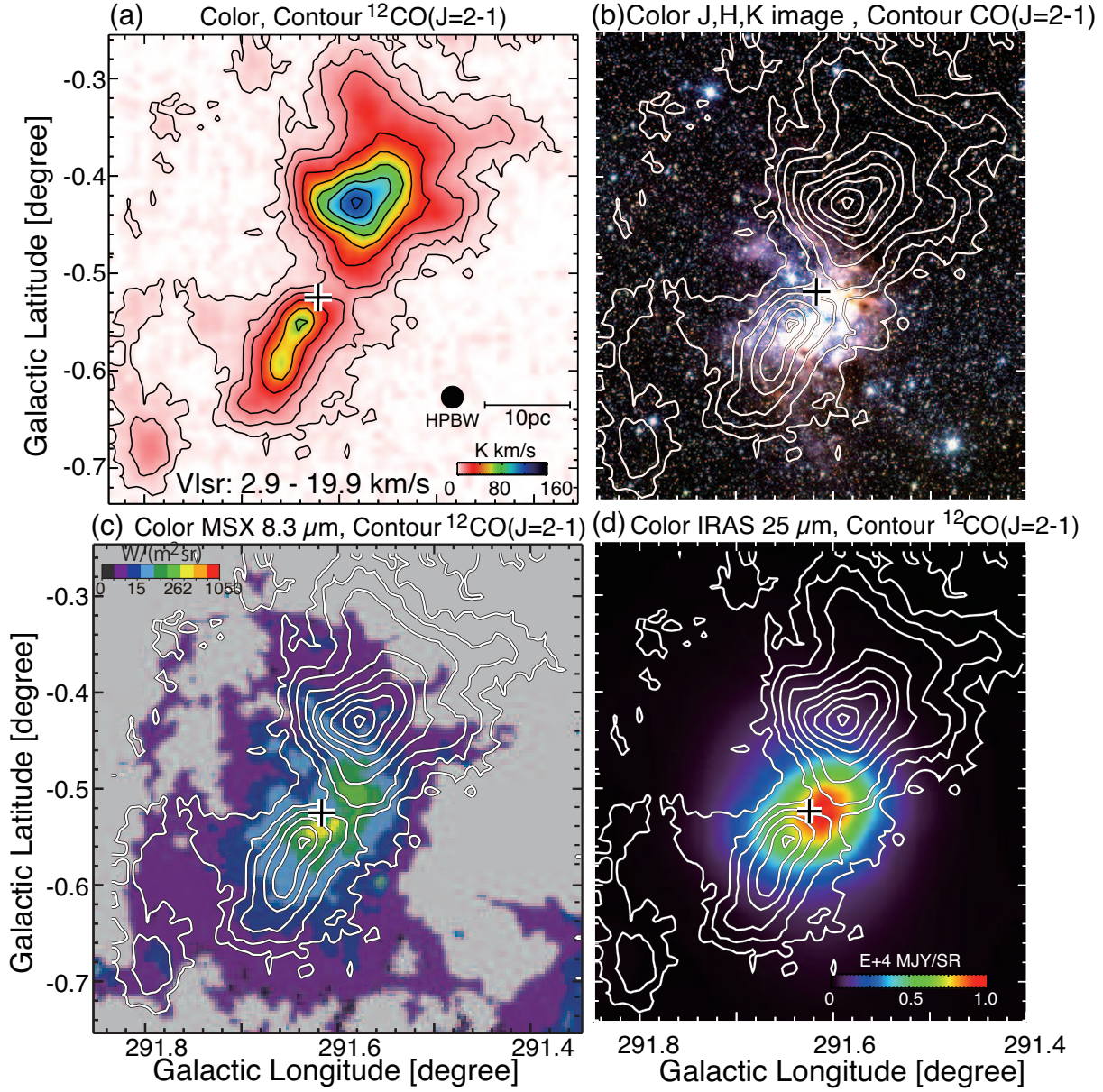


Fig. 7.— (a) Distribution of $^{12}\text{CO}(J=2-1)$ integrated intensity with the velocity range from 2.9 km s^{-1} to 19.9 km s^{-1} . Contours are plotted at levels of (2.5, 7.0, 15, 30, 50, 70, 90) K km s^{-1} . A cross depicts the central cluster. (b) $^{12}\text{CO}(J=2-1)$ distribution of the molecular clouds associated with NGC3603, superposed on JHK image (Cutri et al. 2003). Blue, yellow and red show J , H , and K bands, respectively. (c) Contour maps of the $^{12}\text{CO}(J=2-1)$ emission superposed on the MSX 8.3 μm image (Wang & Chen 2010). The cross depicts the central cluster. (d) Contour maps of the $^{12}\text{CO}(J=2-1)$ emission superposed on $IRAS$ 25 μm data.

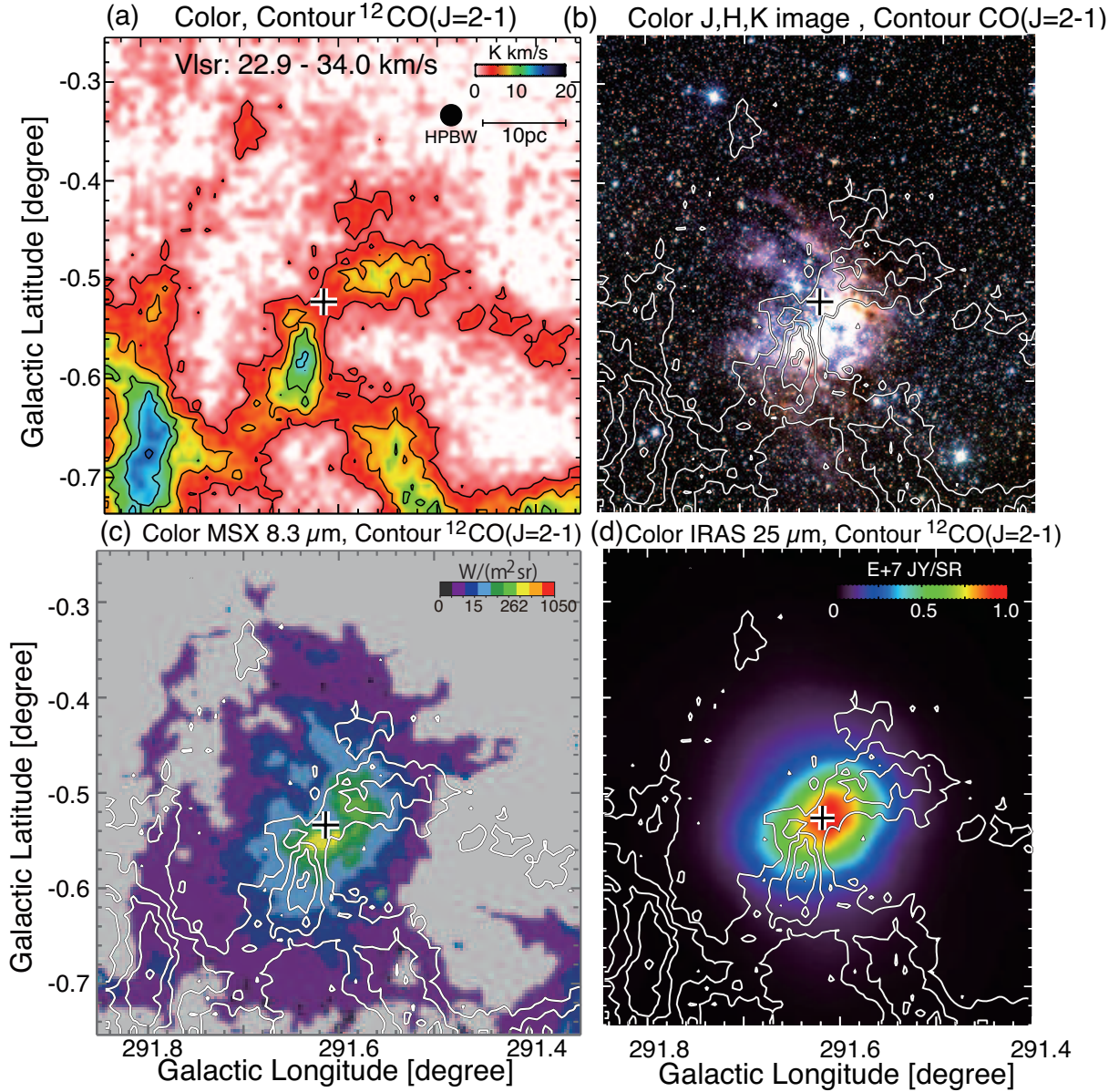


Fig. 8.— (a) Distribution of $^{12}\text{CO}(J=2-1)$ integrated intensity with the velocity range from 22.9 km s^{-1} to 34.0 km s^{-1} . Contours are plotted every 3.0 K km s^{-1} from 3.0 K km s^{-1} . A cross depicts the central cluster. (b) $^{12}\text{CO}(J=2-1)$ distribution of the molecular clouds associated with NGC3603, superposed on JHK image (Cutri et al. 2003). Blue, yellow and red show J , H , and K bands, respectively. (c) Contour maps of the $^{12}\text{CO}(J=2-1)$ emission superposed on the MSX $8.3 \mu\text{m}$ image (Wang & Chen 2010). The cross depicts the central cluster. (d) Contour maps of the $^{12}\text{CO}(J=2-1)$ emission superposed on IRAS $25 \mu\text{m}$ data.

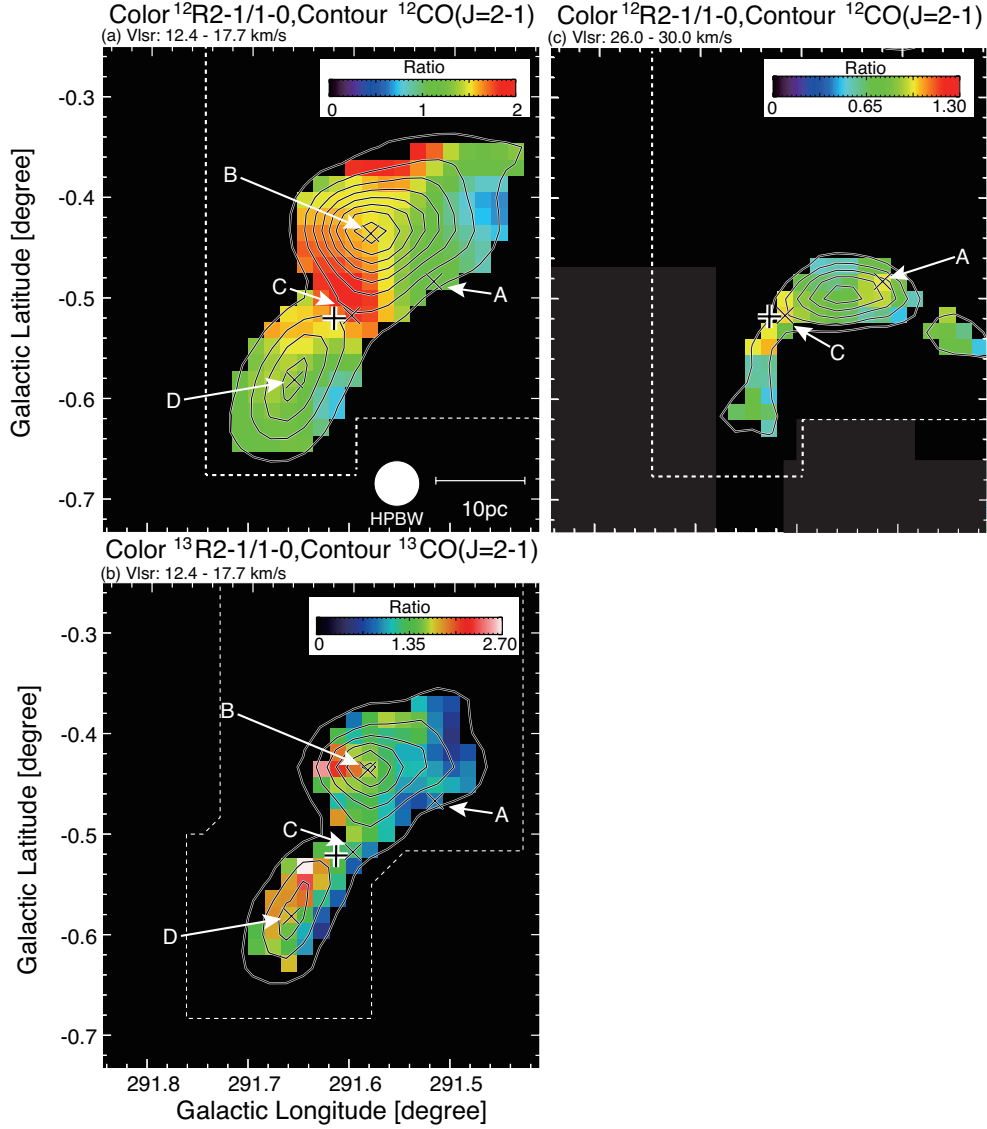


Fig. 9.— (a) Distribution of the ratio of $^{12}\text{CO}(J=2-1)$ and $^{12}\text{CO}(J=1-0)$ integrated intensity in the range 12.4 km s⁻¹ to 17.7 km s⁻¹. Contours show the $^{12}\text{CO}(J=2-1)$ emission smoothed with a Gaussian function to a 156'' spatial resolution and are plotted every 4.5 K km s⁻¹ from 4.5 K km s⁻¹. (b) Distribution of the ratio of $^{13}\text{CO}(J=2-1)$ and $^{13}\text{CO}(J=1-0)$ integrated intensity in the range 1.0 km s⁻¹ to 2.5 km s⁻¹. (c) Distribution of the ratio of $^{12}\text{CO}(J=2-1)$ and $^{12}\text{CO}(J=1-0)$ integrated intensity in the range 27.6 km s⁻¹ to 34.3 km s⁻¹. The cross corresponds to the position of the cluster NGC3603. Points A–D show the locations of the CO spectra in Figure 10 and LVG analysis in Figure 11.

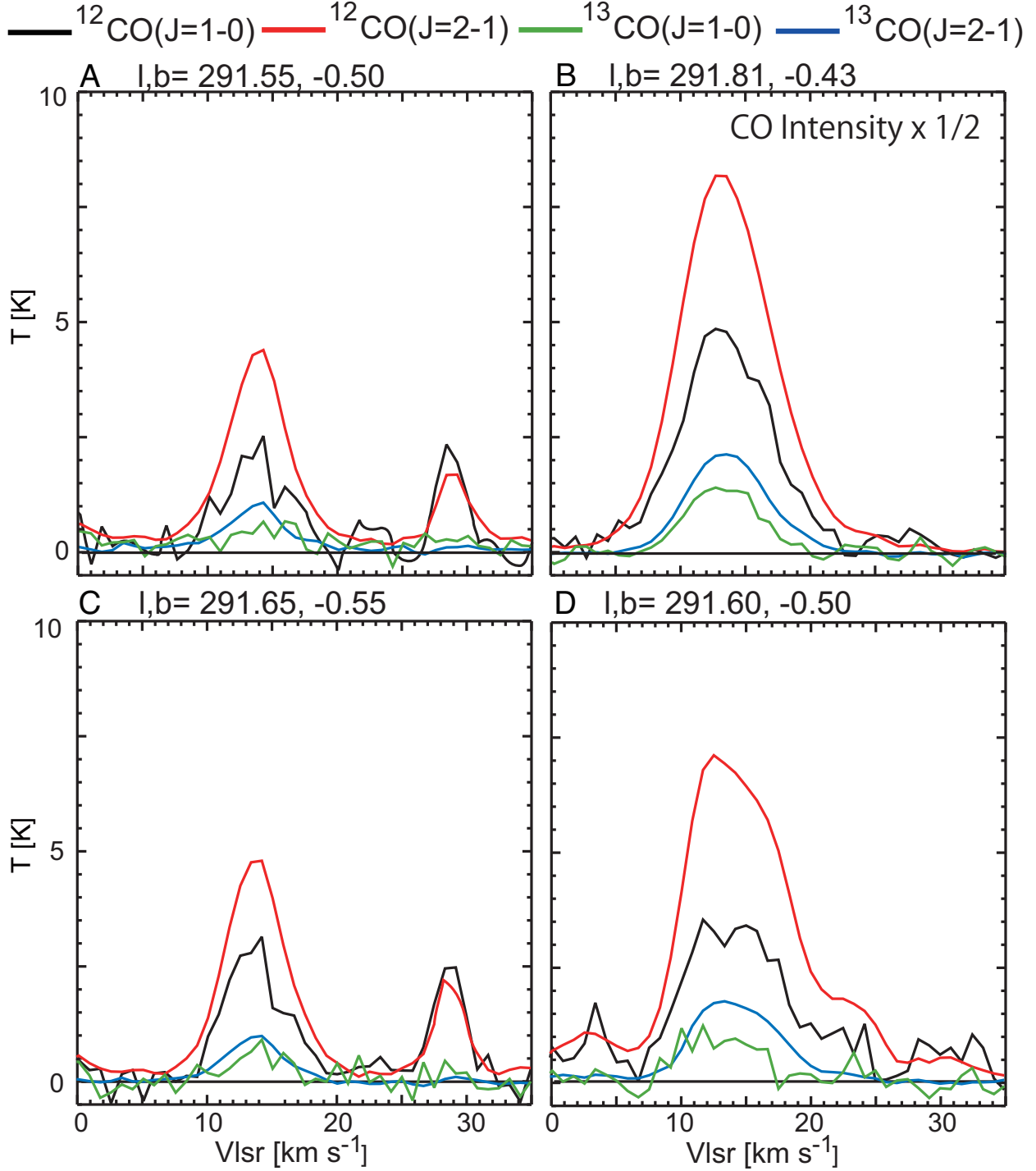


Fig. 10.— CO spectra at the peak positions of the clouds shown in Figure 9. CO intensity is plotted at half of its true value for point B. $^{12}\text{CO}(J=1-0)$, $^{12}\text{CO}(J=2-1)$, $^{13}\text{CO}(J=1-0)$ and $^{13}\text{CO}(J=2-1)$ are plotted in black, red, green and blue, respectively. All spectra were smoothed to be a beam size of $2''.6$.

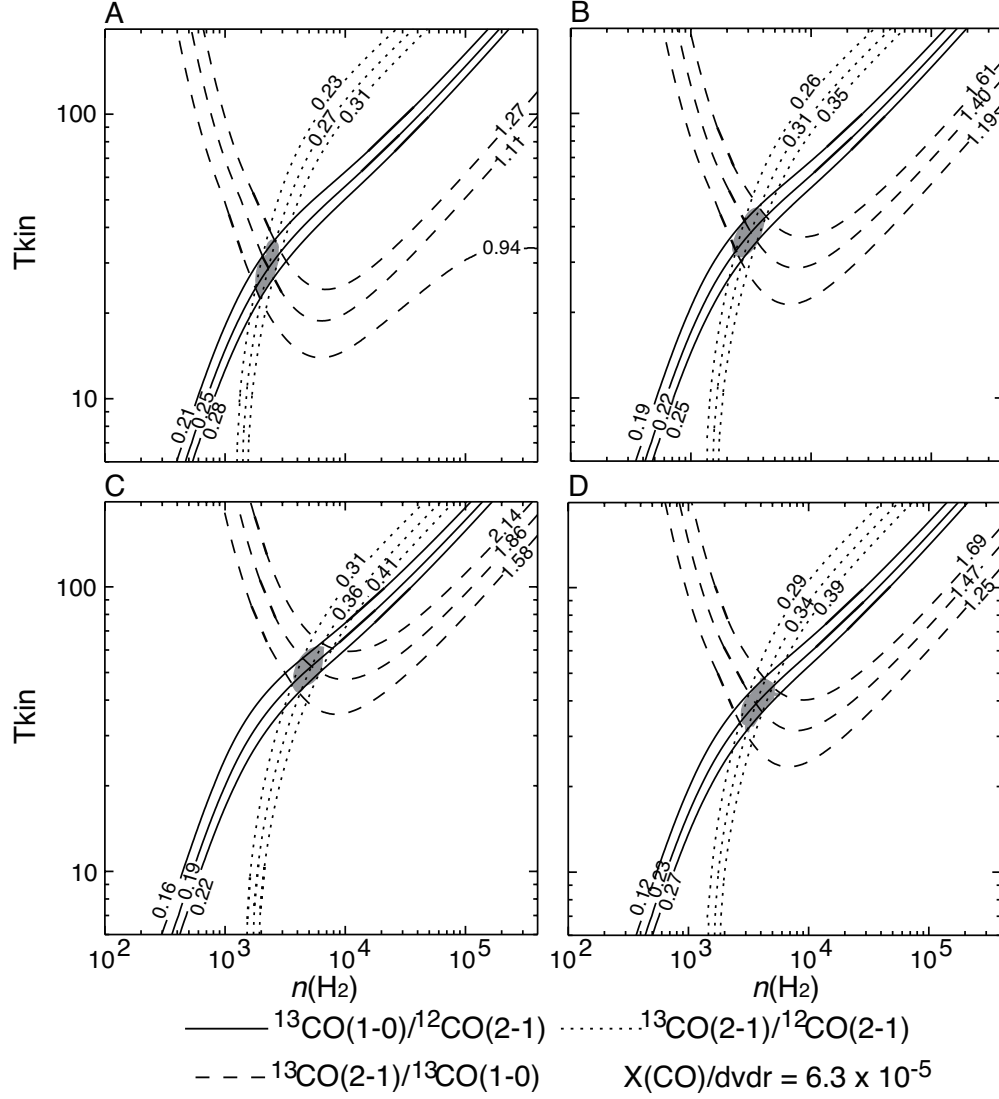


Fig. 11.— LVG results for $X(\text{CO})/(dv/dr) = 6.3 \times 10^{-5} \text{ (km s}^{-1} \text{ pc}^{-1})^{-1}$, assuming a distance of 7.0 kpc, are shown in the density-temperature plane. Solid, dotted, and dashed lines show $^{13}\text{CO}(J=1-0)/^{12}\text{CO}(J=2-1)$, $^{13}\text{CO}(J=2-1)/^{12}\text{CO}(J=2-1)$, and $^{13}\text{CO}(J=2-1)/^{13}\text{CO}(J=1-0)$ intensity ratios.

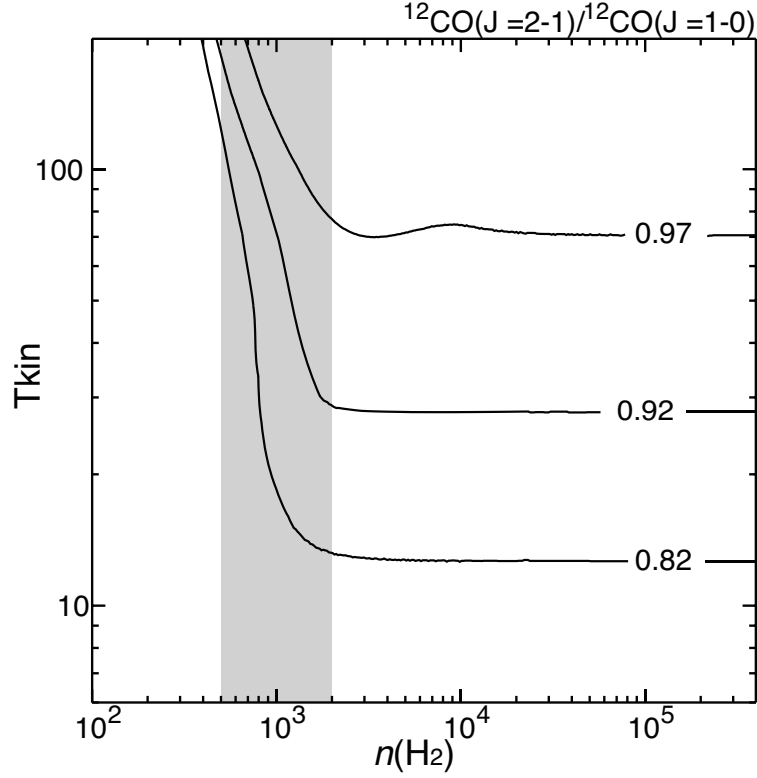


Fig. 12.— LVG results for $X(\text{CO})/(dv/dr) = 6.3 \times 10^{-5} (\text{km s}^{-1} \text{pc}^{-1})^{-1}$, assuming a distance of 7.0 kpc, are shown in the density-temperature plane. Solid lines show $^{12}\text{CO}(J=2-1)/^{12}\text{CO}(J=1-0)$ intensity ratios at the position of the red-shifted cloud toward NGC3603. Gray shows the probable range of number density estimated by the molecular column density and the cloud width.

Table 1. Properties of the super star clusters in the Galaxy.

Name	l [degree]	b [degree]	D [kpc]	Age [Myr]	$\log(M_{\text{phot}}/M_{\odot})$	Radius [pc]	IR nebulosities	Reference ¹	Reference ²
Arches	0.12	0.02	8.0	2.0	4.3	0.4	No	1	
Quintuplet	0.16	−0.06	8.2	4.0	4.0	2.0	No	2	
RCW38	268.03	−0.98	1.7	≤1.0	—	0.8	Yes	3	
Westerlund 2	284.25	−0.40	5.4	2.0	4.0	0.8	Yes	4	8
Trumpler 14	287.41	−0.58	2.6	2.0	4.0	0.5	No	5	
NGC3603	291.62	−0.52	7.0	2.0	4.1	0.7	Yes	6	previous work
Westerlund 1	339.55	−0.40	5.2	3.5	4.5	1.0	No	7	
[DBS2003]179	347.58	0.19	7.9	3.5	3.8	1.2	Yes	4	

Note. — Column 1: name of cluster; Columns 2 and 3: position of cluster; Column 4: distance; Column 5: age of cluster; Column 6: mass of cluster; Column 7: radius of cluster; Column 8: comment; Column 9: reference¹ shows paper of clusters; 1, Figer et al. (1999); 2, Figer et al. (1999); 3, Mizutani et al. (1987); 4, Pfalzner (2009); 5, Ascenso et al. (2007); 6, Harayama et al.

(2008); 7, Clark et al. (2010, 2005); reference² shows paper of molecular clouds; 8 Furukawa et al. (2009b); Ohama et al. (2010)

Table 2. Observed properties of the blue-shifted cloud and the red-shifted cloud.

Name	l	b	W [$^{12}\text{CO}(J=1-0)$]	N_{H_2}	A_V	A_J	A_H	A_K
	[degree]	[degree]	[K km s $^{-1}$]	[10^{21} cm $^{-2}$]	[mag]	[mag]	[mag]	[mag]
Blue-shifted Cloud North	291.58	−0.42	150	30	31.8	9.0	6.0	3.6
Blue-shifted Cloud South	291.64	−0.55	80	16	17.0	4.8	3.2	1.9
Red-shifted Cloud North	291.56	−0.50	6	1.2	1.3	0.4	0.2	0.1
Red-shifted Cloud South	291.64	−0.58	12	2.4	2.5	0.7	0.5	0.3

Note. — Column 1: name of the cloud. Columns 2 and 3: peak position of the cloud. Column 4: integrated intensity of the $^{12}\text{CO}(J=1-0)$ emission. Column 5: molecular column density. Column 6: visual extinction given by $A_V/N_{\text{H}} = 5.3 \times 10^{-22} \text{ mag cm}^2 \text{ H}^{-1}$ (Bohlin et al. 1978) and $N_{\text{H}_2} = 2N_{\text{H}}$. Here we assumed $R_V = A_V/E(B-V) = 3.1$. Column 7 – 9 : extinction at J ($1.2 \mu\text{m}$), H ($1.7 \mu\text{m}$), and K ($2.2 \mu\text{m}$) bands, respectively. Here we adopted an extinction law of Cardelli et al. (1989); $A_J/A_V = 0.28$, $A_H/A_V = 0.19$, and $A_K/A_V = 0.11$.

Table 3. Results of the LVG analysis.

Name	Positon	l	b	V_{lsr}	R_1	R_2	T_{kin}	$n(\text{H}_2)$
		[deg]	[deg]	[km s ⁻¹]			[K]	[cm ⁻³]
Blue-shifted cloud	A	291.55	-0.50	12.4–17.7	1.11	0.70	29_{-7}^{+9}	$2.3_{-0.5}^{+0.9} \times 10^3$
	B	291.58	-0.43	12.4–17.7	1.40	1.26	28_{-9}^{+10}	$3.2_{-2.0}^{+1.8} \times 10^3$
	C	291.31	-0.50	12.4–17.7	1.86	1.45	53_{-11}^{+12}	$5.2_{-2.2}^{+4.8} \times 10^3$
	D	291.66	-0.58	12.4–17.7	1.47	1.81	39_{-9}^{+11}	$3.6_{-0.4}^{+3.4} \times 10^3$
Red-shifted cloud	C	291.60	-0.50	26.0–30.0	0.92	—	$\leq 70^*$	$\geq 10^{3\dagger}$
	D	291.66	-0.58	26.0–30.0	0.82	—	$\leq 20^*$	$\geq 10^{3\dagger}$

Note. — Column 1: name of the cloud; Column 2: observed points of the cloud; Column 3: galactic longitude of the peak position; Column 4: galactic latitude of the peak position; Column 5: range of velocity integrated; Column 6: ratio of $^{12}\text{CO}(J=2-1)/^{12}\text{CO}(J=1-0)$; Column 7: ratio of $^{13}\text{CO}(J=2-1)/^{13}\text{CO}(J=1-0)$; Column 8: kinetic temperature; Column 9: number density of H_2 . * lower limit † upper limit

Table 4. Physical parameters of the molecular clouds.

Name	Mass	R
	$[10^4 M_{\odot}]$	[pc]
Blue-shifted cloud	7.2	
North	5.5	12.3
South	1.7	8.4
Red-shifted cloud	1.2	
North	0.4	5.1
South	0.8	6.9

Note. — Column 1: name of the cloud; Column 2: position of the cloud; Column 3: cloud mass derived using an X -factor of $2.0 \times 10^{20} \text{ cm}^{-2} (\text{K km s}^{-1})^{-1}$; Column 4: radius of the cloud